Sparsity-Driven ISAR Imaging Based on Two-Dimensional ADMM

1 author:

Hamid Reza Hashempour
Shiraz University
10 PUBLICATIONS   **72** CITATIONS

Sparsity-Driven ISAR Imaging Based on Two-Dimensional ADMM

Hamid Reza Hashempour

Abstract—Compressed sensing (CS) can achieve high resolution inverse synthetic aperture radar (ISAR) imaging of moving targets with limited measurements. Recently, alternating direction method of multipliers (ADMM) has been introduced to solve the optimization problem for one dimensional (1D) sparse signal recovery. The main drawback of 1D sparsity-driven algorithms are the high memory usage and the computational complexity. Thus, in this paper a novel two dimensional (2D) ADMM approach is presented which can be directly applied to the ISAR model in matrix form, and needs lower memory and computations compared to the 1D algorithm. Moreover, the performance of the 2D-ADMM method is better than the 2D smoothed L0 (2D-SL0) and 2D gradient projection sequential order one negative exponential (2D-GP-SOONE) algorithms in different signal-to-noise ratio (SNR) conditions and sampling rates. Joint simulations and measured data results based on real data of Yak-42 airplane, validate the superiority of the proposed approach.

Index Terms—Inverse synthetic aperture radar (ISAR), alternating direction method of multipliers (ADMM), sparse matrix recovery, two dimensional compressed sensing (2D-CS)

I. Introduction

Inverse synthetic aperture radar (ISAR) is an effective signal processing tool which can obtain high resolution images of moving targets from all-day and all-weather environment. ISAR widely applied in various military and civilian applications, e.g., target identification and classification, air/space surveillance, etc. [1], [2]. In order to attain high resolution ISAR images in range and cross-range directions, wide bandwidth signal and long coherent processing interval (CPI) are required, respectively. However, by increasing the radar bandwidth and CPI, the amount of data increased significantly, which causes a big problem in data acquisition and storage system. On the other hand, in a long CPI, the assumption of constant rotation rate of the target is not valid, which degrades the ISAR image obtained from the conventional range-Doppler Algorithm (RDA).

Compressed sensing (CS), as an emerging technique in signal processing, states that a high-dimensional unknown sparse or compressible signal can be reconstructed exactly from limited measurement with overwhelming probability by solving a sparsity-driven optimization problem [3]–[6]. CS has been widely exploited and developed in radar imaging because of intrinsic sparsity of ISAR images, and can achieve high resolution images with limited measurements [7]–[13]. In [7], a CS-based approach is presented to achieve high resolution with limited pulses. The problem of ISAR imaging based

on CS from incomplete data is also considered in [9]. The problem of sparse vector recovery can be solved by several methods, e.g., basis pursuit [14], matching pursuit [15], and smoothed L0 (SL0) [16]. However, the aforementioned methods cannot be directly used to solve a sparse matrix. In [17] a 2D-SL0 algorithm has been proposed, which could be applied directly to 2D signals. Based on 2D-SL0, a 2D compressive sensing (2D-CS) algorithm for high resolution ISAR imaging is presented in [10]. A gradient projection sequential order one negative exponential (GP-SOONE) method is introduced in [11] to solve a constrained nonconvex problem and reconstruct the sparse signal. This method has been further developed for matrix recovery and the 2D-GP-SOONE algorithm has been exploited for high resolution ISAR imaging of maneuvering targets [12], [13].

Alternating direction method of multipliers (ADMM), is a proximal splitting algorithm which can solve non-smooth and large-scale optimization problems [18]–[20]. ADMM uses auxiliary variables and divides the problem to individual convex sub-problems which are solved easily based on proximal operators. In this paper, based on this method, first a one dimensional ADMM (1D-ADMM) approach for ISAR imaging is presented, then a generalized 2D-ADMM algorithm which can directly reconstruct sparse matrices is proposed. The presented 2D approach has a lower computational complexity and requires less memory storage for computation compared to the 1D-ADMM method. Furthermore, 2D-ADMM is more robust to noise than the 2D-SL0 and 2D-GP-SOONE algorithms. We also develop our algorithm for 2D-CS to reconstruct ISAR images from undersampled data in both range and cross-range directions. Several simulations and measured data of Yak-42 aircraft, are exploited to validate the effectiveness of the proposed algorithm for super-resolution ISAR imaging from complete and undersampled data acquisition cases.

The remainder of this paper is organized as follows. Section II introduces the signal model. Section III presents the proposed 1D and 2D-ADMM ISAR imaging methods. Then, simulated and real data are utilized to validate the efficiency and superiority of the proposed approach in section IV. Eventually, section V concludes this study.

II. Signal model

In ISAR imaging, the instantaneous range of a target includes rotational and translational motions, which the former provides the essential angular diversity to achieve cross-range resolution, and the latter is undesired and in this paper, it is assumed to be compensated completely by conventional

The author is with the School of Electrical and Computer Engineering, Shiraz University, Shiraz 7134851154, Iran e-mail: hrhashempour@shirazu.ac.ir.
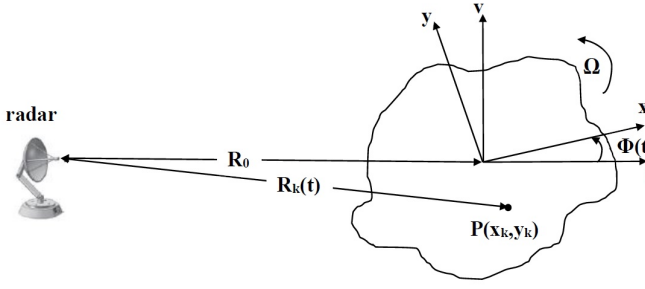
Fig. 1. Geometry of a rotating target in ISAR model

motion compensation methods such as [2], [21]. Therefore, after removing the translational motion, it is supposed that the target is uniformly rotating as shown in Fig. 1.

After range compression, the received signal from the target can be expressed as follows:

$$s(f_m, t_n) = \sum_{k=1}^{K} \sigma_k \cdot \exp\left\{\frac{-j4\pi f_m R_k(t_n)}{c}\right\} + z(f_m, t_n) \quad (1)$$

where $z(f_m, t_n)$ is the additive white Gaussian noise after range compression. f_m denotes the range-frequency and defined as: $f_m = f_c + (m-1)\Delta f$, $m = -(M-1)/2, \ldots, M/2$, f_c is the carrier frequency and Δf is the space between two samples in the frequency domain. t_n stands for discrete slow time and $n = 1, 2, \ldots, N$ is the number of pulses. K is the number of scattering centers in the target, σ_k denotes the radar cross section (RCS) coefficient of the kth scatterer, c is the speed of light, and $R_k(t_n)$ is the instantaneous distance from the kth scatterer to the radar. In ISAR imaging, the target is usually assumed to be in the far field, so $R_k(t)$ can be approximated as

$$R_k(t_n) \cong R_0 + x_k \cos(\Omega t_n) - y_k \sin(\Omega t_n) \quad (2)$$

where R_0 and Ω are the target's initial range distance from the radar and the rotation rate of the target, respectively. When the CPI or the rotation rate or both are sufficiently small, $R_k(t)$ can be approximated as:

$$R_k(t) \approx R_0 + x_k - y_k \Omega t_n \quad (3)$$

By substituting (3) into (1), neglecting the constant phase term, and compensating the migration through resolution cells (MTRC) [22], we have:

$$s(f_m, t_n) = \sum_{k=1}^{K} \sigma_k \cdot \exp\left\{\frac{-j4\pi f_m x_k}{c}\right\}$$
$$\cdot \exp\left\{\frac{j4\pi f_c y_k \Omega t_n}{c}\right\} + z(f_m, t_n) \quad (4)$$

The target scene can be represented as a 2D matrix $\mathbf{X}$ with the size of $P \times Q$ where $p = 1, 2, \ldots, P$ and $q = 1, 2, \ldots, Q$ are the number of pixels along y and x axis, respectively. Then, equation (4) can be written in matrix form as:

$$\mathbf{S} = \mathbf{F}_a \mathbf{X} \mathbf{F}_r^T + \mathbf{Z} \quad (5)$$

where $(\cdot)^T$ stands for transpose of a matrix. $\mathbf{S} \in \mathbb{C}^{N \times M}$ and

$\mathbf{Z} \in \mathbb{C}^{N \times M}$ represent the received signal and the complex Gaussian noise matrix, respectively. $\mathbf{F}_a \in \mathbb{C}^{N \times P}$ and $\mathbf{F}_r \in \mathbb{C}^{M \times Q}$ express the partial Fourier matrices in the azimuth and range directions, respectively, which are given by

$$\mathbf{F}_a = \begin{bmatrix} 1 & 1 & \cdots & 1 \\ 1 & \omega & \cdots & \omega^{(P-1)} \\ \vdots & \vdots & \ddots & \vdots \\ 1 & \omega^{(N-1)} & \cdots & \omega^{(N-1)(P-1)} \end{bmatrix}, \omega = \exp\left(-j\frac{2\pi}{N}\right) \quad (6)$$

$$\mathbf{F}_r = \begin{bmatrix} 1 & 1 & \cdots & 1 \\ 1 & \nu & \cdots & \nu^{(Q-1)} \\ \vdots & \vdots & \ddots & \vdots \\ 1 & \nu^{(M-1)} & \cdots & \nu^{(M-1)(Q-1)} \end{bmatrix}, \nu = \exp\left(-j\frac{2\pi}{M}\right) \quad (7)$$

In order to have supper-resolution ISAR images, N and M should be smaller than P and Q, respectively.

III. PROPOSED METHOD

In this section, first, an ADMM-based approach for sparse recovery is derived, then the method is developed for the 2D model of (5). Finally, the proposed algorithm is generalized for 2D undersampling.

A. ADMM-based ISAR imaging

Conventional sparsity-driven algorithms cannot be directly applied to matrix representation, as in (5). Thus, in CS, the sparse matrix is stacked to a single column vector to recover uniquely from an underdetermined linear system [3], [4]. By utilizing Kronecker products, the 2D ISAR model in (5) is equivalently expressed in vector form as:

$$\mathbf{s} = \mathbf{\Phi}\mathbf{x} + \mathbf{z} \quad (8)$$

where $\mathbf{s} = \text{vect}(\mathbf{S})$, $\mathbf{x} = \text{vect}(\mathbf{X})$, $\mathbf{z} = \text{vect}(\mathbf{Z})$, $\mathbf{\Phi} = \mathbf{F}_r \otimes \mathbf{F}_a$, $\otimes$ denotes the Kronecker product, and $\text{vect}(\cdot)$ represents stacking columns of a matrix into a vector one after the other.

The sparse vector $\mathbf{x}$ in (8) can be recovered by solving the following optimization problem

$$\hat{\mathbf{x}} = \arg\min_{\mathbf{x}} \frac{1}{2}\|\mathbf{s} - \mathbf{\Phi}\mathbf{x}\|_2^2 + \lambda\|\mathbf{x}\|_1 \quad (9)$$

where $\|\cdot\|_2$ represents the Euclidean norm of a vector. To solve (9), an algorithm based on ADMM is derived. In ADMM, the problem must be reformulated by introducing a new variable

$$\hat{\mathbf{x}}, \hat{\mathbf{b}} = \arg\min_{\mathbf{x},\mathbf{b}} \frac{1}{2}\|\mathbf{s} - \mathbf{\Phi}\mathbf{x}\|_2^2 + \lambda\|\mathbf{b}\|_1 \quad \text{s.t.} \quad \mathbf{x} = \mathbf{b} \quad (10)$$

The associated augmented Lagrangian (AL) function is

$$\mathcal{L}_\delta^A(\mathbf{x}, \mathbf{b}, \mathbf{u}) = \frac{1}{2}\|\mathbf{s} - \mathbf{\Phi}\mathbf{x}\|_2^2 + \lambda\|\mathbf{b}\|_1$$
$$+ \Re\left\{\mathbf{u}^H(\mathbf{x} - \mathbf{b})\right\} + \frac{\delta}{2}\|\mathbf{x} - \mathbf{b}\|_2^2 \quad (11)$$

where $\mathbf{u}$ and δ are the Lagrange multiplier and the penalty parameter, respectively. ADMM minimizes $\mathcal{L}_\delta^A$ over $\mathbf{x}, \mathbf{b}, \mathbf{u}$

separately, leading to sub-problems. Therefore, the scaled form of ADMM reads

$$\mathbf{x}_{j+1} = \arg\min_{\mathbf{x}} \frac{1}{2} \|\mathbf{s} - \mathbf{\Phi}\mathbf{x}\|_2^2 + \frac{\delta}{2} \|\mathbf{x} - \mathbf{b}_j + \mathbf{v}_j\|_2^2 \quad (12)$$

$$\mathbf{b}_{j+1} = \arg\min_{\mathbf{b}} \frac{\lambda}{\delta} \|\mathbf{b}\|_1 + \frac{1}{2} \|\mathbf{x}_{j+1} - \mathbf{b} + \mathbf{v}_j\|_2^2 \quad (13)$$

$$\mathbf{v}_{j+1} = \mathbf{v}_j + \mathbf{x}_{j+1} - \mathbf{b}_{j+1} \quad (14)$$

where $(\cdot)^H$ denotes the Hermitian transpose of a matrix and $\mathbf{v}_j = \delta^{-1}\mathbf{u}_j$ is called the scaled dual variable. The minimization of the quadratic functions in (12) can easily be solved by taking the first derivative. The solution of the l_1 norm in (13) can be obtained by using proximal operators. A proximal operator of g with parameter ρ can be defined as

$$\text{prox}_{\rho g}(\mathbf{z}) = \arg\min_{\mathbf{x}} \frac{1}{2} \|\mathbf{x} - \mathbf{z}\|_2^2 + \rho g(\mathbf{x}) \quad (15)$$

For some choices of g, well-known closed form of the so-called mforeau proximal mapping (MPM) function exists. For example, when $g(\mathbf{x}) = \|\mathbf{x}\|_1$, then the solution can be achieved by soft-thresholding function: $\mathcal{S}_\rho(\mathbf{z}) = \text{sgn}(\mathbf{z}) \cdot \max(|\mathbf{z}| - \rho, 0)$. Therefore, the solution for each of the optimization problems in (12)-(14) can be obtained through the following equations:

$$\mathbf{x}_{j+1} = \left(\mathbf{\Phi}^H\mathbf{\Phi} + \delta\mathbf{I}\right)^{-1}\left(\mathbf{\Phi}^H\mathbf{s} + \delta(\mathbf{b}_j - \mathbf{v}_j)\right) \quad (16)$$

$$\mathbf{b}_{j+1} = \mathcal{S}_{\lambda/\delta}(\mathbf{x}_{j+1} + \mathbf{v}_j) \quad (17)$$

$$\mathbf{v}_{j+1} = \mathbf{v}_j + \mathbf{x}_{j+1} - \mathbf{b}_{j+1} \quad (18)$$

Note that, although (16) has analytical solution, the computation of matrix inverse is impractical for large values of $\mathbf{I}$. Therefore, a Conjugate-Gradient (CG) algorithm with warm starting is exploited in [23] to solve this subproblem. However, applying CG algorithm is also time consuming. Here, we want to further simplify (16) based on the matrix inversion lemma. $\mathbf{F}_a$ and $\mathbf{F}_r$ are partial Fourier matrices with $N < P$ and $M < Q$, which satisfy the $\mathbf{F}_a\mathbf{F}_a^H = \mathbf{I}$, and $\mathbf{F}_r\mathbf{F}_r^H = \mathbf{I}$, respectively. Therefore, $\mathbf{\Phi}\mathbf{\Phi}^H$ can be written as:

$$\begin{aligned}
\mathbf{\Phi}\mathbf{\Phi}^H &= (\mathbf{F}_r \otimes \mathbf{F}_a)(\mathbf{F}_r \otimes \mathbf{F}_a)^H \\
&= (\mathbf{F}_r \otimes \mathbf{F}_a)(\mathbf{F}_r^H \otimes \mathbf{F}_a^H) \\
&= (\mathbf{F}_r\mathbf{F}_r^H) \otimes (\mathbf{F}_a\mathbf{F}_a^H) \\
&= \mathbf{I}. \quad (19)
\end{aligned}$$

Using (19) and the Woodbury matrix identity, we have

$$\begin{aligned}
\left(\mathbf{\Phi}^H\mathbf{\Phi} + \delta\mathbf{I}\right)^{-1} &= \frac{1}{\delta}\left(\mathbf{I} - \mathbf{\Phi}^H(\mathbf{\Phi}\mathbf{\Phi}^H + \delta\mathbf{I})^{-1}\mathbf{\Phi}\right) \\
&= \frac{1}{\delta}\left(\mathbf{I} - \frac{1}{1+\delta}\mathbf{\Phi}^H\mathbf{\Phi}\right). \quad (20)
\end{aligned}$$

Based on (20), and after simple manipulation, the equation (16) can be rewritten as:

$$\mathbf{x}_{j+1} = (\mathbf{b}_j - \mathbf{v}_j) - \frac{1}{1+\delta}\mathbf{\Phi}^H\left(\mathbf{\Phi}(\mathbf{b}_j - \mathbf{v}_j) - \mathbf{s}\right) \quad (21)$$

Therefore, the cost of (21) is the products by $\mathbf{\Phi}^H$ and $\mathbf{\Phi}$. If we use the fast Fourier transform (FFT) algorithm instead of matrix multiplication, the cost is of order $O(n\log n)$ operations.

Based on above solutions for each step, the proposed 1D-

ADMM ISAR imaging procedure is demonstrated in Algorithm 1.

Algorithm 1 The 1D-ADMM algorithm for ISAR imaging

1: **Input:** $\mathbf{s}, \delta > 0, \lambda \geq 0$
2: **Initialization:** $j = 0, \mathbf{x}_0 = \mathbf{b}_0 = \mathbf{v}_0 = \mathbf{0}$.
3: **while** stopping criterion is not met **do**
4: $\quad \mathbf{x}_{j+1} = (\mathbf{b}_j - \mathbf{v}_j) - \frac{1}{1+\delta}\mathbf{\Phi}^H\left(\mathbf{\Phi}(\mathbf{b}_j - \mathbf{v}_j) - \mathbf{s}\right)$
5: $\quad \mathbf{b}_{j+1} = \mathcal{S}_{\lambda/\delta}(\mathbf{x}_{j+1} + \mathbf{v}_j)$
6: $\quad \mathbf{v}_{j+1} = \mathbf{v}_j + \mathbf{x}_{j+1} - \mathbf{b}_{j+1}$
7: **end while**
8: **Output:** $\hat{\mathbf{x}} = \mathbf{x}_j$

It is worth noting that Algorithm 1 is stopped if a predefined maximum number of iterations is reached, or if the corresponding objective function does not decrease significantly any more, i.e. when $\|\mathbf{x}_{j+1} - \mathbf{x}_j\|_2 / \|\mathbf{x}_j\|_2 < \epsilon$, where ϵ is a small positive number.

The computational complexity of the 1D-ADMM algorithm is dominated by step 4 in Algorithm 1. The matrix-vector multiplications with the assumption of $P = Q$ require $O(P^4MN + P^4 + P^2MN)$ computations. Since $M, N < P$, the complexity is in the order of $O(P^4MN)$. Thus, 1D-ADMM is feasible only when P,M,N are fairly small.

B. 2D-ADMM Algorithm

In this section, we want to generalize Algorithm 1 to obtain the 2D-ADMM method for sparse matrix recovery. The equivalent matrix form of the l_1 minimization problem of (9) is as follows:

$$\hat{\mathbf{X}} = \arg\min_{\mathbf{X}} \frac{1}{2}\left\|\mathbf{S} - \mathbf{F}_a\mathbf{X}\mathbf{F}_r^T\right\|_F^2 + \lambda\|\mathbf{X}\|_1 \quad (22)$$

where λ is a regularization parameter and $\|\cdot\|_F$ is the Frobenius norm. It is worth mentioning that, the matrix $\mathbf{\Phi} \in \mathbb{C}^{MN \times PQ}$ has much more elements than $\mathbf{F}_a$ and $\mathbf{F}_r$. Thus, solving the 2D problem in (22) which requires much smaller memory is more efficient than the 1D optimization in (9).

In order to obtain the 2D-ADMM algorithm, first, the equivalent matrix form of step 4 in Algorithm 1 is derived. Assume that $\mathbf{b} = \text{vect}(\mathbf{B})$ and $\mathbf{v} = \text{vect}(\mathbf{V})$, then we have:

$$\begin{aligned}
&(\mathbf{\Phi}^H\mathbf{\Phi})(\mathbf{b} - \mathbf{v}) - \mathbf{\Phi}^H\mathbf{s} \\
&= (\mathbf{F}_r^H \otimes \mathbf{F}_a^H)(\mathbf{F}_r \otimes \mathbf{F}_a)\text{vect}(\mathbf{B} - \mathbf{V}) - (\mathbf{F}_r^H \otimes \mathbf{F}_a^H)\text{vect}(\mathbf{S}) \\
&= (\mathbf{F}_r^H\mathbf{F}_r) \otimes (\mathbf{F}_a^H\mathbf{F}_a)\text{vect}(\mathbf{B} - \mathbf{V}) - (\mathbf{F}_r^H \otimes \mathbf{F}_a^H)\text{vect}(\mathbf{S}) \\
&= \text{vect}(\mathbf{F}_a^H\mathbf{F}_a(\mathbf{B} - \mathbf{V})\mathbf{F}_r^T\mathbf{F}_r^* - \mathbf{F}_a^H\mathbf{S}\mathbf{F}_r^*) \\
&= \text{vect}\left(\mathbf{F}_a^H(\mathbf{F}_a(\mathbf{B} - \mathbf{V})\mathbf{F}_r^T - \mathbf{S})\mathbf{F}_r^*\right). \quad (23)
\end{aligned}$$

where $(\cdot)^*$ stands for complex conjugate of a matrix. Therefore the equivalent matrix form of step 4 in Algorithm 1 is obtained as:

$$\mathbf{X}_{j+1} = (\mathbf{B}_j - \mathbf{V}_j) - \frac{1}{1+\delta}\mathbf{F}_a^H(\mathbf{F}_a(\mathbf{B}_j - \mathbf{V}_j)\mathbf{F}_r^T - \mathbf{S})\mathbf{F}_r^* \quad (24)$$

Then, the matrix representation of step 5 in Algorithm 1 is given by:

$$\mathbf{B}_{j+1} = \mathcal{S}_{\lambda/\delta}(\mathbf{X}_{j+1} + \mathbf{V}_j) \qquad (25)$$

where $\mathcal{S}_\rho(\mathbf{Z})$ denotes an element wise operation with $\mathcal{S}_\rho(\mathbf{Z}) = \text{sgn}(\mathbf{Z}_{nm}) \cdot \max(|\mathbf{Z}_{nm}| - \rho, 0)$ for all indices n, m of the $N \times M$ matrix $\mathbf{Z}$. These steps lead to the 2D-ADMM algorithm, as a generalization of 1D-ADMM with matrix inputs, which is given in Algorithm 2.

Algorithm 2 The 2D-ADMM algorithm for ISAR imaging

1: **Input:** $\mathbf{S}, \delta > 0, \lambda \geq 0$
2: **Initialization:** $j = 0, \mathbf{X}_0 = \mathbf{B}_0 = \mathbf{V}_0 = \mathbf{0}$.
3: **while** stopping criterion is not met **do**
4: $\quad \mathbf{X}_{j+1} = (\mathbf{B}_j - \mathbf{V}_j) - \dfrac{1}{1+\delta}\mathbf{F}_a^H(\mathbf{F}_a(\mathbf{B}_j - \mathbf{V}_j)\mathbf{F}_r^T - \mathbf{S})\mathbf{F}_r^*$
5: $\quad \mathbf{B}_{j+1} = \mathcal{S}_{\lambda/\delta}(\mathbf{X}_{j+1} + \mathbf{V}_j)$
6: $\quad \mathbf{V}_{j+1} = \mathbf{V}_j + \mathbf{X}_{j+1} - \mathbf{B}_{j+1}$
7: **end while**
8: **Output:** $\hat{\mathbf{X}} = \mathbf{X}_j$

Similar to Algorithm 1, the stopping criteria of Algorithm 2 is met when either $\|\mathbf{X}_{j+1} - \mathbf{X}_j\|_F / \|\mathbf{X}_j\|_F < \xi$, where ξ is a small positive number, or the number of iterations reaches a predefined limit. The computational complexity of Algorithm 2, is also dominated by step 4. The matrix-matrix multiplication at step 4 in Algorithm 2 with the assumption of $P = Q$ is performed with $O(P^2(P + N + 3M) + PMN)$ computations. Since $M, N < P$, the worst case complexity is $O(P^3)$. Recall, that 1D-AMM has worst case complexity of $O(P^4MN)$. Thus, there is a $O(PMN)$ gain in the matrix version compared to the vector approach. Consequently, Algorithms 1 and 2 have the same output, however, Algorithm 2 is more efficient.

Let us compare the computational complexity of Algorithm 2 with 2D-SL0 and 2D-GP-SOONE. The most expensive computational operation of both 2D-SL0 and 2D-GP-SOONE in each iteration, is to compute the following equation [12], [17]:

$$\mathbf{X}_{j+1} = \mathbf{X}_j - \mathbf{F}_a^\dagger(\mathbf{F}_a\mathbf{X}_j\mathbf{F}_r^T - \mathbf{S})(\mathbf{F}_r^\dagger)^T \qquad (26)$$

where $(\cdot)^\dagger$ denotes the pseudo-inverse of a matrix and is computed as:

$$\mathbf{F}_a^\dagger = \mathbf{F}_a^H(\mathbf{F}_a\mathbf{F}_a^H)^{-1} = \mathbf{F}_a^H \qquad (27)$$

In a similar manner we have: $\mathbf{F}_r^\dagger = \mathbf{F}_r^H$, and consequently (26) is simplified to:

$$\mathbf{X}_{j+1} = \mathbf{X}_j - \mathbf{F}_a^H(\mathbf{F}_a\mathbf{X}_j\mathbf{F}_r^T - \mathbf{S})\mathbf{F}_r^* \qquad (28)$$

By comparing (28) with step 4 in Algorithm 2, it is observed that 2D-SL0, 2D-GP-SOONE and 2D-ADMM have the same worst-case complexity i.e. $O(P^3)$. However, the run time of the algorithms are not necessary the same, since the other steps and the number of iterations required for convergence of each algorithm are different.

C. Generalizing to 2D-CS

Let us consider the sparsely sampled signal reconstruction. The observation matrix for the 1D model has the form $\boldsymbol{\Psi}\boldsymbol{\Phi}$, where $\boldsymbol{\Psi}$ is an $L_1L_2 \times MN$ binary matrix, where $L_1(L_1 < M)$ and $L_2(L_2 < N)$ are the sparsely sampled numbers in the range and cross-range directions, respectively, and $\boldsymbol{\Psi}$ can be obtained by taking a subset of rows of an identity matrix. Due to its particular structure, this matrix satisfies $\boldsymbol{\Psi}\boldsymbol{\Psi}^T = \mathbf{I}$. Similar to (20), based on this fact and using the Woodbury matrix identity, we have

$$\left(\boldsymbol{\Phi}^H\boldsymbol{\Psi}^H\boldsymbol{\Psi}\boldsymbol{\Phi} + \delta\mathbf{I}\right)^{-1} = \frac{1}{\delta}\left(\mathbf{I} - \frac{1}{1+\delta}\boldsymbol{\Phi}^H\boldsymbol{\Psi}^T\boldsymbol{\Psi}\boldsymbol{\Phi}\right). \quad (29)$$

Therefore, according to (29), step 4 in Algorithm 1, is modified as:

$$\mathbf{x}_{j+1} = (\mathbf{b}_j - \mathbf{v}_j) - \frac{1}{1+\delta}\boldsymbol{\Phi}^H\boldsymbol{\Psi}^T\left(\boldsymbol{\Psi}\boldsymbol{\Phi}(\mathbf{b}_j - \mathbf{v}_j) - \mathbf{s}\right) \qquad (30)$$

For the matrix form in Algorithm 2, similarly step 4 can be derived as:

$$\mathbf{X}_{j+1} = (\mathbf{B}_j - \mathbf{V}_j) - \\ \frac{1}{1+\delta}\mathbf{F}_a^H\boldsymbol{\Psi}_a^T(\boldsymbol{\Psi}_a\mathbf{F}_a(\mathbf{B}_j - \mathbf{V}_j)\mathbf{F}_r^T\boldsymbol{\Psi}_r^T - \mathbf{S})\boldsymbol{\Psi}_r\mathbf{F}_r^* \quad (31)$$

where $\boldsymbol{\Psi}_a$ with the size of $L_2 \times N$ and $\boldsymbol{\Psi}_r$ with the size of $L_1 \times M$ are the sensing matrices in the cross-range and range directions, respectively, and $\boldsymbol{\Psi} = \boldsymbol{\Psi}_r \otimes \boldsymbol{\Psi}_a$.

IV. EXPERIMENTAL RESULTS

A. Simulated data

In this section the performance of the proposed 2D-ADMM algorithm is evaluated using synthetic data. The radar parameters are shown in Table I. The scene size is 50×50, with 11 ideal point-like targets. The 2D-FFT, 2D-SL0, 2D-GP-SOONE and 2D-ADMM algorithms have been applied to the simulated data to form the ISAR images. The target scene is displayed in Fig.2a. The normalized mean square error (NMSE) between the estimated ISAR image and the target scene defined as $\text{NMSE}_{\mathbf{X}} = 10\log_{10}\|\hat{\mathbf{X}}/|\hat{\mathbf{X}}|_{\max} - \mathbf{X}/|\mathbf{X}|_{\max}\|_F^2$, is used to quantitatively compare the different algorithms.

In order to achieve super-resolution ISAR images, we set $P = 2N$ and $Q = 2M$, (i.e. $P = Q = 100$) in this simulation. By adding complex Gaussian noise, raw data is generated for signal-to-noise ratios (SNR) from -10 to $30dB$. For example, in SNR=-10 dB, the acquired ISAR images by the different methods are shown in Figs. 2b-2e. Furthermore, the $\text{NMSE}_{\mathbf{X}}$ of the aforementioned algorithms for the different SNR levels is shown in Fig. 2f. Observing the obtained ISAR images (Figs. 2b-2e) and the $\text{NMSE}_{\mathbf{X}}$ diagram (Fig. 2f), it can be understood that the proposed approach outperforms the other ones in all SNR levels.

In the next simulation, we compare the algorithms for 2D-CS. Fig. 3 demonstrates the ISAR images obtained by 2D-GP-SOONE, 2D-SL0 and 2D-ADMM in udersampling ratio (MN/PQ) of 0.1 for SNR =-5 and 5dB. Some artificial points exist in the imaging results of 2D-GP-SOONE and 2D-SL0.

TABLE I
RADAR PARAMETERS FOR SIMULATED DATA

Carrier frequency f_c	10 GHz
Bandwidth B	500 MHz
Pulse Repetition Frequency PRF	50 Hz
Number of range cells M	50
Number of pulses N	50

Fig. 3. The ISAR images obtained by 2D-GP-SOONE, 2D-SL0 and 2D-ADMM in undersampling ratio of 0.1 for SNR =-5 dB ((a)-(c)) and SNR =5 dB ((d)-(f)), respectively

Fig. 2. (a) Original target scene. The obtained ISAR images using (b) 2D-FFT, (c) 2D-GP-SOONE, (d) 2D-SL0 and (e) 2D-ADMM for SNR =-10 dB. (f) NMSE$_\mathbf{X}$ of different methods versus different SNR levels.

Fig. 4. NMSE$_\mathbf{X}$ obtained from different methods as undersampling ratio is varied for (a) SNR = 10, (b) 5, and (c) 0 dB.

However, compared to them, our algorithm can achieve better image quality in both SNR levels. Moreover, the NMSE$_\mathbf{X}$ of different methods versus undersampling ratio of 0.1 to 1, is depicted in Fig. 4 for SNR levels of 10, 5 and 0 dB. It is seen that NMSE$_\mathbf{X}$ of 2D-ADMM in all cases is lower than that of the other methods. When the sampling ratio approaches 1, the performance of 2D-SL0 and 2D-GP-SOONE are reduced and in sampling ratio of 1, the MSEs of them are equal to that of 2D-FFT. However, for 2D-AMM, by increasing the udersampling ratio the performance is improved significantly which again validates the superiority of the proposed algorithm.
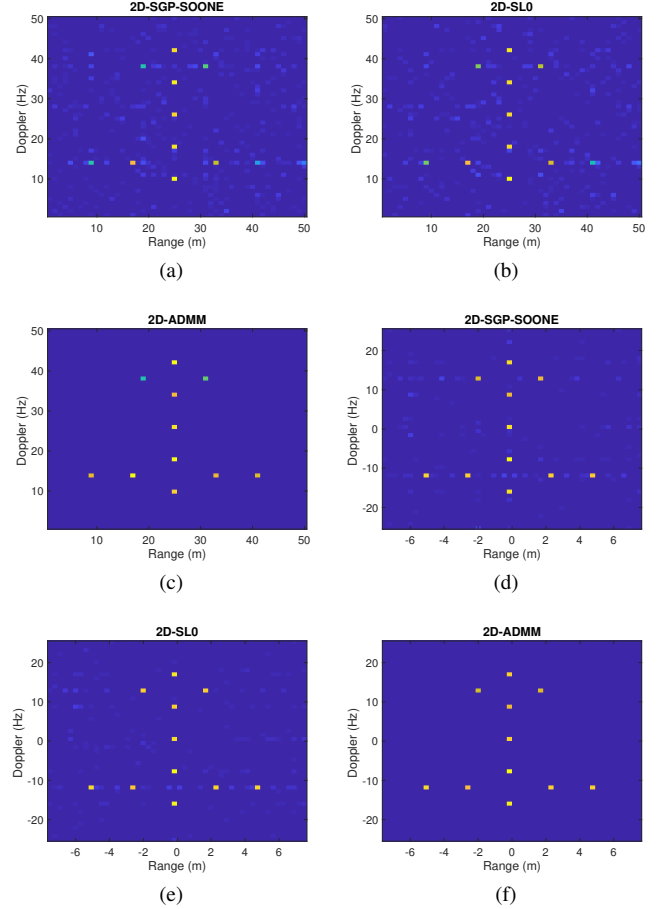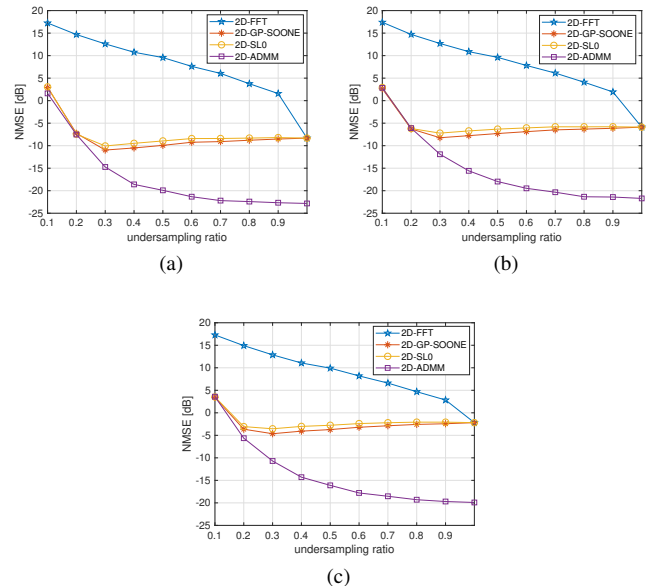
TABLE II
ENTROPY OF THE ISAR IMAGE FOR DIFFERENT ALGORITHMS

Algorithm	SNR = 10dB	SNR = 5dB	SNR = 0dB
2D-FFT	6.86	7.72	8.98
2D-GP-SOONE	5.24	5.93	7.20
2D-SL0	4.70	5.32	6.60
2D-ADMM	4.27	4.30	4.31

B. Real data

In this subsection, the measured data set of the Yak-42 aircraft, is utilized to further validate the effectiveness of the proposed algorithm. The measured data set is collected by a radar with a central frequency, bandwidth and duration of 5.52 GHz, 400 MHz and 25.6 μs, respectively. The target is a Yak-42 aircraft sized $24m \times 24m$. The complete radar echo contains 256 pulses, and each pulse consists of 256 samples.

In Fig. 5 the ISAR images of Yak-42 exploited from different methods are demonstrated. The number of pulses (N), and the range cells (M) are 64 and 256, respectively. In order to have super-resolution ISAR images, we set P=2N and Q=2M. The first, second and third rows of Fig. 5 are obtained under SNR levels of 10, 5 and 0 dB, respectively. From Fig. 5, it is obvious that the images obtained from the 2D-FFT have the lowest quality, and 2D-ADMM have the best performance in all SNR cases. Although, 2D-SL0 and 2D-GP-SOONE have good results in SNR=10 dB, their performance reduced dramatically in low SNR conditions. Table II shows the entropy values of the ISAR images in Fig. 5 to quantitatively compares the performance of the algorithms. The image entropy is defined as [2]

$$IE_x = -\sum_{p=1}^{P}\sum_{q=1}^{Q} \frac{|\mathbf{X}_{p,q}|^2}{E} \log \frac{|\mathbf{X}_{p,q}|^2}{E} \tag{32}$$

where $E = \sum_{p=1}^{P}\sum_{q=1}^{Q} |\mathbf{X}_{p,q}|^2$ is the image energy. Generally, a well-focused image has a low entropy value. As it can be seen, the image entropy of the proposed algorithm in all cases is the lowest compared to the others.

For the last experiment, we consider 2D-CS, i.e. the algorithms are compared for different sampling rates of 12.5, 25, 50 and 75%. In this experiment, we set P=Q=256, and the performance of algorithms is considered for SNR=10 dB (Fig. 6) and 0 dB (Fig. 7). The undersampling is achieved by randomly selecting the rows of the Fourier matrices in both range and cross-range directions. Fig. 6 shows that in low sampling rates the performance of all approaches are near together, but in the higher sampling rates 2D-ADMM yields better results comparing to 2D-SL0 and 2D-GP-SOONE. Fig. 7 displays similar results for SNR=0 dB. As expected in low SNR conditions, the proposed method outperforms the others in all sampling rate schemes, i.e. is more robust to noise compared to the 2D-SL0 and 2D-GP-SOONE algorithms. Furthermore, in order to have a quantitative comparison, the entropy values of the ISAR images in Figs. 6 and 7 are demonstrated in Table III. Clearly, the proposed method has the lowest entropy in all conditions.

TABLE III
ENTROPY OF THE ISAR IMAGE OBTAINED FROM DIFFERENT ALGORITHMS FOR DIFFERENT SAMPLING RATES

Scheme	Sampling rate	12.5%	25%	50%	75%
	2D-GP-SOONE	5.92	6.11	6.36	6.50
SNR= 10 dB	2D-SL0	5.32	5.65	6.15	6.46
	2D-ADMM	4.40	4.69	4.97	5.19
	2D-GP-SOONE	6.74	7.41	8.05	8.52
SNR= 0 dB	2D-SL0	6.49	7.04	7.89	8.48
	2D-ADMM	4.45	4.70	5.04	5.40

Consequently, the results obtained from both simulated and real data, validate the superiority of the proposed algorithm.

V. CONCLUSION

In this paper, a 2D-ADMM method for sparse matrix recovery and high resolution ISAR imaging was proposed, which is more computationally efficient compared to solving the 1D optimization and requires lower memory during computation. Moreover, compared to 2D-FFT, 2D-GP-SOONE and 2D-SL0, the performance of the proposed approach is better in different SNR levels and undersampling ratios. Both simulations and real data were utilized to show the superiority of the proposed method.

In this paper the phase error was not considered. Thus, future works will focus on developing the algorithm for ISAR autofocusing.

REFERENCES

[1] C. Ozdemir, *Inverse Synthetic Aperture Radar Imaging with MATLAB Algorithms*, New Jersey: John Wiley and Sons, Inc., 2012.

[2] H. R. Hashempour, M. A. Masnadi-Shirazi, "Inverse synthetic aperture radar phase adjustment and cross-range scaling based on sparsity," *Digital Signal Processing*, Vol. 68, pp. 93-101, 2017.

[3] E. Candes, J. Romberg, and T. Tao, "Robust uncertainty principles: exact signal reconstruction from highly incomplete frequency information,"*IEEE Trans. Inf. Theory*, vol. 52, no. 2, pp. 489-509, Feb. 2006.

[4] D. Donoho, "Compressed sensing," *IEEE Trans. Inf. Theory*, vol. 52, no. 4, pp. 12891306, Apr. 2006.

[5] E. J. Candes and M. B. Wakin, "An introduction to compressive sampling," *IEEE Signal Processing Magazine*, vol. 25, no. 2, pp. 21-30, March 2008.

[6] E. Cands and T. Tao, "Near optimal signal recovery from random projections: Universal encoding strategies?" *IEEE Trans. Inf. Theory*, vol. 52, no. 12, pp. 54065425, Dec. 2006.

[7] L. Zhang, M. D. Xing, C. W. Qiu, J. Li, and Z. Bao, "Achieving higher resolution ISAR imaging with limited pulses via compressed sampling," *IEEE Geosci. Remote Sens. Lett.*, vol. 6, no. 3, pp. 567-571, Jul. 2009.

[8] E. Giusti, Q. Wei, A. Bacci, S. Tomei and M. Martorella, "Super resolution ISAR imaging via Compressing Sensing," *EUSAR 2014; 10th European Conference on Synthetic Aperture Radar*, Berlin, Germany, 2014, pp. 1-4.

[9] S. Tomei, A. Bacci, E. Giusti, M. Martorella, and F. Berizzi, "Compressive sensing-based inverse synthetic radar imaging from incomplete data, *IET Radar Sonar Navig.*, vol. 10, no. 2, pp. 386-397, 2016.

[10] H. R. Hashempour, M. A. Masnadi-Shirazi and B. Abbasi Arand, "Compressive Sensing ISAR imaging with LFM signal," *2017 Iranian Conference on Electrical Engineering (ICEE)*, Tehran, 2017, pp. 1869-1873.

[11] C. Ma, T. S. Yeo, Y. Zhao and J. Feng, "MIMO radar 3D imaging based on combined amplitude and total variation cost function with sequential order one negative exponential form," *IEEE Transactions on Image Processing*, vol. 23, no. 5, pp. 2168-2183, May 2014.
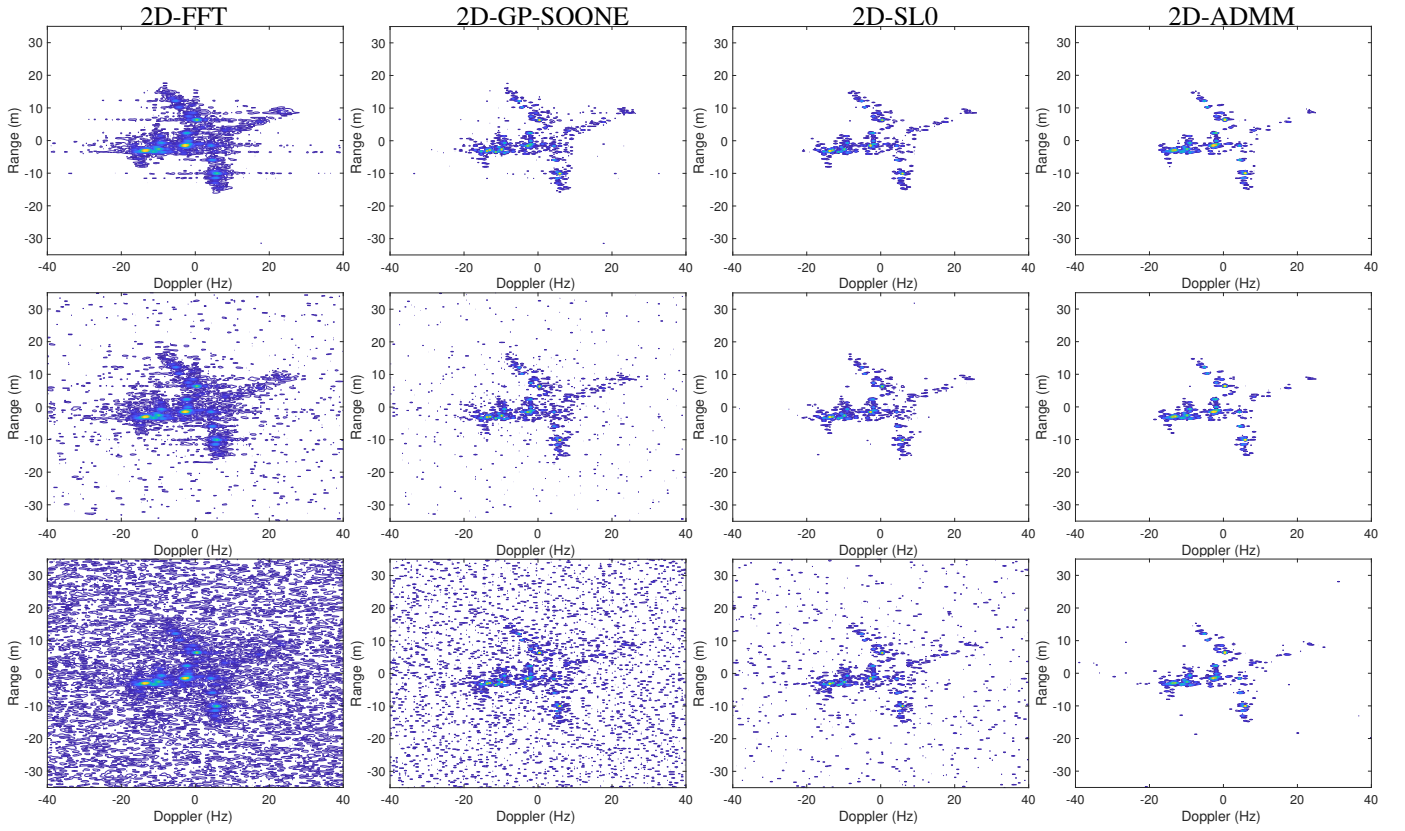
Fig. 5. ISAR images of Yak-42 obtained from different methods for N=64, M=256, P=2N and Q=2M. From top to bottom SNR = 10, 5 and 0 dB, respectively.
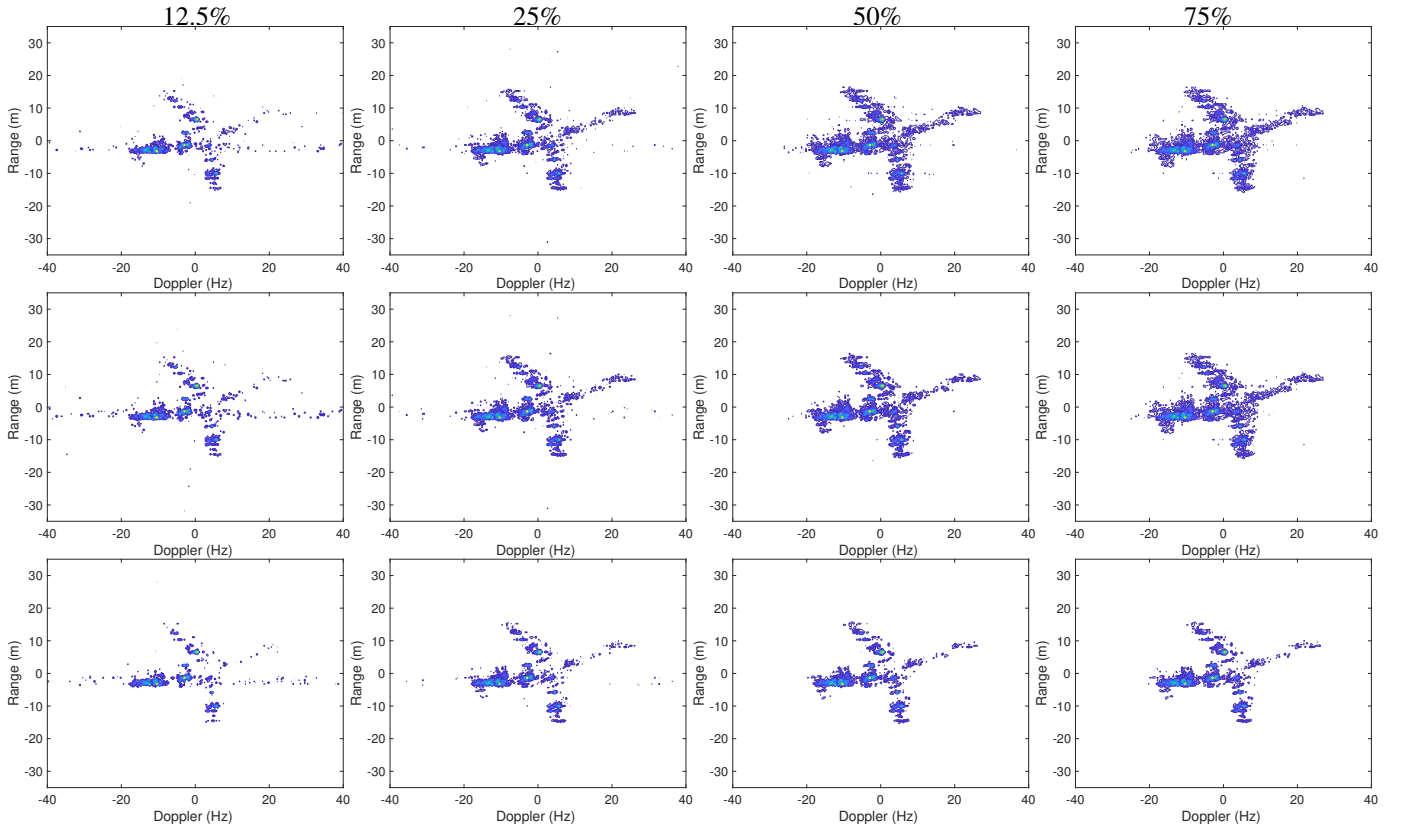

Fig. 6. From top to bottom ISAR images of Yak-42 obtained from 2D-GP-SOONE, 2D-SL0 and 2D-ADMM for different sampling rates. (SNR =10 dB and P=Q=256)
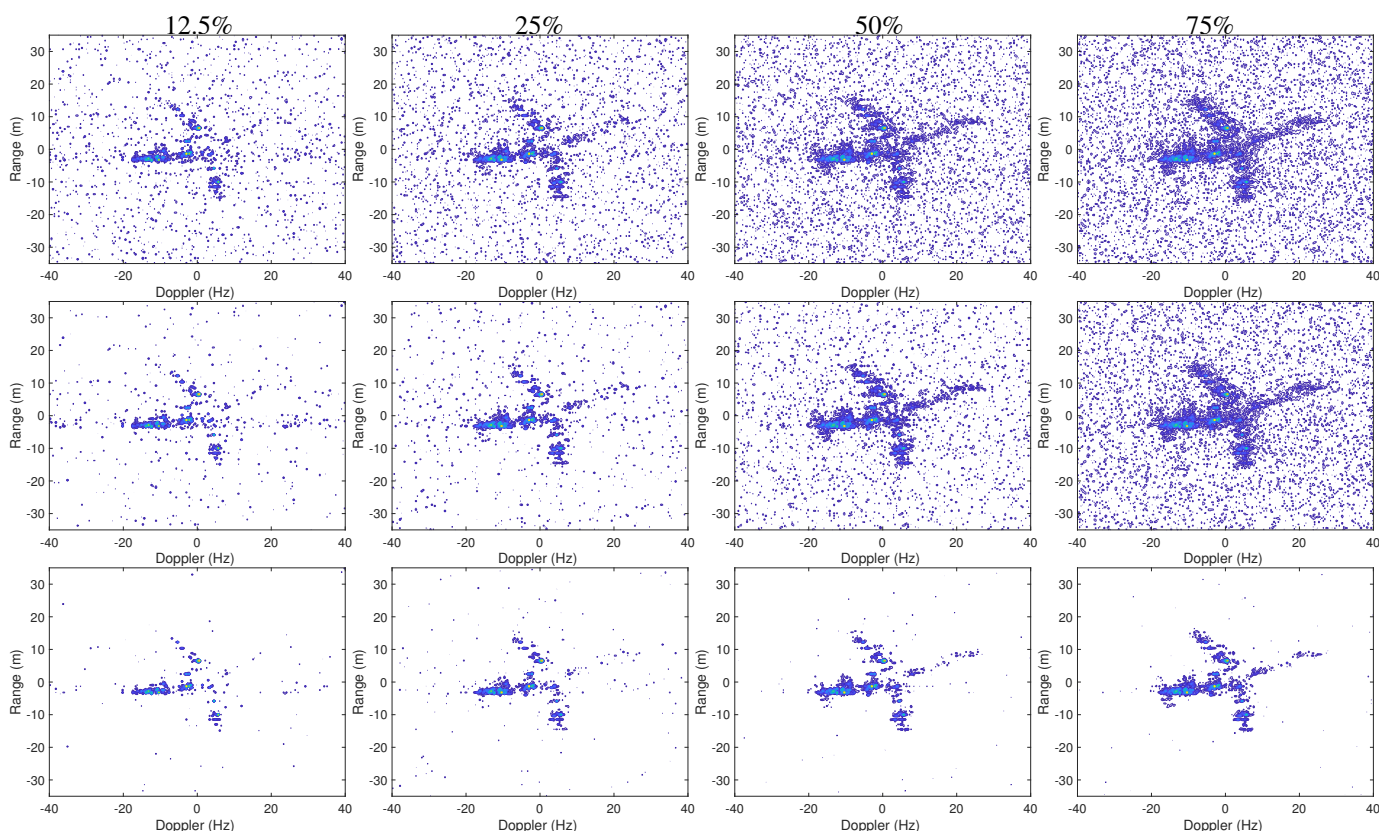
Fig. 7. From top to bottom ISAR images of Yak-42 obtained from 2D-GP-SOONE, 2D-SL0 and 2D-ADMM for different sampling rates. (SNR =0 dB and P=Q=256)

[12] X. He, N. Tong and X. Hu, "Dynamic ISAR imaging of maneuvering targets based on sparse matrix recovery," *Signal Processing*, vol. 134, pp. 123-129, 2017.

[13] H. R. Hashempour and A. Sheikhi, "Dynamic ISAR imaging and auto-focusing of maneuvering targets based on sequential GPSOONE method and eigenvalue decomposition," *IEEE Sensors Journal*, vol. 19, no. 11, pp. 4045-4053, June, 2019.

[14] S. Chen, D. Donoho, and M. Saunders, "Atomic decomposition by basis pursuit," *SIAM J. Sci. Comput*, vol. 20, no. 1, pp. 33-61, 1998.

[15] S. Mallat, and Z. Zhang, "Matching pursuits with timefrequency dictionaries," *IEEE Trans. Signal Process.*, vol. 41, no. 12, pp. 3397-3415, 1993.

[16] H. Mohimani, M. Babaie-Zadeh and C. Jutten, "A fast approach for overcomplete sparse decomposition based on smoothed ℓ^0 norm," *IEEE Transactions on Signal Processing*, vol. 57, no. 1, pp. 289-301, Jan. 2009.

[17] A. Ghaffari, M. Babaie-Zadeh and C. Jutten, "Sparse decomposition of two dimensional signals," *2009 IEEE International Conference on Acoustics, Speech and Signal Processing*, Taipei, 2009, pp. 3157-3160.

[18] N. Parikh, and S. Boyd., "Proximal algorithms," *Foundations and Trends® in Optimization*, vol. 1, no. 3, pp. 127-239, 2014

[19] P. L. Combettes, and J.-C. Pesquet, "Proximal splitting methods in signal processing", *Fixed-Point Algorithms for Inverse Problems in Science and Engineering*, pp. 185-212, 2011

[20] S. Boyd, et al, "Distributed optimization and statistical learning via the alternating direction method of multipliers", *Foundations and Trends® in Machine learning*, Vol. 3, No. 1, pp. 1-122, 2011

[21] H. R. Hashempour, M. A. Masnadi-Shirazi, and A. Sheikhi, "Cyclic Prefix-Based OFDM ISAR Imaging," *Iranian Journal of Science and Technology*, Vol. 42, No. 2, pp. 239-249, 2018

[22] M. Xing, R. Wu, J. Lan, and Z. Bao, "Migration through resolution cell compensation in ISAR imaging," *IEEE Geosci. Remote Sens. Lett.*, vol. 1, no. 2, pp. 141144, Apr. 2004.

[23] M. Moradikia, S. Samadi, and M. Cetin, "Joint SAR imaging and multi-feature decomposition from 2-D under-sampled data via low-rankness plus sparsity priors", *IEEE Trans. Comput. Imaging*,vol. 5, no. 1, pp. 1-16, 2018.

Hamid Reza Hashempour was born in 1987. He received the B.S., M.S., and Ph.D. degrees in electrical engineering from Shiraz University, Shiraz, Iran in 2009, 2011, and 2017, respectively.

His current research interests include radar signal processing, radar imaging (SAR/ISAR), and compressive sensing.